Tellus SERIES A DYNAMIC METEOROLOGY AND OCEANOGRAPHY
PUBLISHED BY THE INTERNATIONAL METEOROLOGICAL INSTITUTE IN STOCKHOLM

# Rotational and divergent kinetic energy in the mesoscale model ALADIN

By V. BLAŽICA[1]*, N. ŽAGAR[1,2], B. STRAJNAR[3] and J. CEDILNIK[3],
[1]*University of Ljubljana, Ljubljana, Slovenia*; [2]*Centre of Excellence SPACE-SI, Ljubljana, Slovenia*; [3]*Slovenian Environment Agency, Ljubljana, Slovenia*

(Manuscript received 7 June 2012; in final form 7 March 2013)

ABSTRACT

Kinetic energy spectra from the mesoscale numerical weather prediction (NWP) model ALADIN with horizontal resolution 4.4 km are split into divergent and rotational components which are then compared at horizontal scales below 300 km and various vertical levels. It is shown that about 50% of kinetic energy in the free troposphere in ALADIN is divergent energy. The percentage increases towards 70% near the surface and in the upper troposphere towards 100 hPa. The maximal percentage of divergent energy is found at stratospheric levels around 100 hPa and at scales below 100 km which are not represented by the global models. At all levels, the divergent energy spectra are characterised by shallower slopes than the rotational energy spectra, and the difference increases as horizontal scales become larger. A very similar vertical distribution of divergent energy is obtained by using the standard ALADIN approach for the computation of spectra based on the extension zone and by applying detrending approach commonly used in mesoscale NWP community.

*Keywords: kinetic energy spectra, rotational energy, divergent energy, ALADIN, limited-area modelling*

## 1. Introduction

Horizontal divergence and convergence patterns have been successfully employed to explain dominant circulation systems on the global and synoptic scales. On these scales, divergence is on average an order of magnitude smaller than the vertical component of vorticity (e.g. Gill, 1982). As the horizontal scale reduces and forcings become more complex, divergence on average increases. On the mesoscale, divergence caused by diabatic heating within convective systems enhances baroclinicity, intensifies the thermally direct mass circulation and generates additional kinetic energy (e.g. Keyser and Johnson, 1984). Nowadays, the life cycle of mesoscale processes such as the organised convection is realistically described by many operational numerical weather prediction (NWP) models that are run at the horizontal grid resolution of a few kilometres.

Divergence and vorticity have also been extensively used in major operational data assimilation systems for NWP both in the global models (Parrish and Derber, 1992; Courtier et al., 1998) and in the models for limited domains (Gustafsson et al., 2001; Fischer et al., 2005). In data assimilation, analysis increments are produced in the model subspace which is spanned by the vorticity and divergence variables instead of the velocity components. Spatial covariances between the forecast errors of prognostic variables are computed for vorticity and divergence and they to a large extent define the spatial structure of the analysis increments and balanced analyses. All in all, it can be argued that divergence is at least equally suitable as vorticity for understanding both flow properties and properties of forecast errors on all spatial scales which are smaller than the Rossby deformation radius, i.e. for unbalanced dynamics (e.g. Gill, 1982). It is thus natural to ask the following questions: what part of kinetic energy is associated with divergence and what with vorticity and how does the energy partitioning between divergent energy and rotational energy change as the horizontal scale becomes smaller at different altitudes?

Divergence is, however, not an observable quantity – it needs to be computed from the velocity components. In the case of global models, the computation of vorticity and divergence can be performed by the application of the Helmholtz theorem. In this way, the kinetic energy spectra obtained as a sum of the zonal and meridional velocity

*Corresponding author.
email: vanja.blazica@fmf.uni-lj.si



Citation: Tellus A 2013, **65**, 18918, http://dx.doi.org/10.3402/tellusa.v65i0.18918

components can easily be replaced by the spectra of divergent and rotational kinetic energy; they describe how the flow variance is split between the balanced (i.e. vorticity dominated) and unbalanced (i.e. divergence dominated) parts as a function of the horizontal wavenumber. The computation is especially elegant in the spectral global models; in this case, the divergent and rotational kinetic energy spectra are obtained from the expansion coefficients of the velocity components in a series of spherical harmonics (e.g. Koshyk and Hamilton, 2001). Koshyk et al. (1999) showed that in several general circulation models divergent and rotational kinetic energy are about equally important in the stratosphere and the mesosphere while in the upper troposphere rotational energy is dominant. A recent evaluation of the European Centre for Medium-Range Weather Forecasts (ECMWF) model spectra at T799 resolution by Burgess et al. (2013) shows that at 200 hPa global divergent energy becomes prevalent over global rotational energy at 400 km whereas above 100 hPa divergent component is dominant over rotational component across all scales smaller than $\sim$1200 km (global wavenumber $\sim$30).

The present paper deals with the computation of rotational and divergent kinetic energy for a limited area model (LAM) with focus on the troposphere. The computation of vorticity and divergence for a limited domain is complicated because the domain boundaries are not periodic, making the application of the Helmholtz theorem difficult (Lynch, 1988, 1989; Li et al., 2006). Consequently, spectra of divergent kinetic energy in limited domains have rarely been used in discussions of mesoscale model circulations. Waite and Snyder (2009) presented such spectra for an idealised simulation of the life cycle of baroclinic wave within a large model domain which allowed the application of periodic boundary conditions in the $x$ direction and a rigid and symmetric boundary condition in the $y$ direction. In agreement with studies based on high-resolution global models, the results showed that divergent kinetic energy dominates in the lower stratosphere while rotational energy prevails in the upper troposphere. In real cases, LAM fields are generally aperiodic and the model equations are solved in the grid-point space. In order to compute the kinetic energy spectra from the velocity components, data are most often made biperiodic by applying the detrending along the rows or columns of the model space followed by the discrete Fourier transform. Errico (1985) and Barnes (1986) presented such a method for a LAM and showed spectra obtained by the summation of the spectral energy density of the zonal and meridional winds over shells in wavenumber space. Skamarock (2004) and Skamarock and Klemp (2008) discussed the kinetic energy spectra for the Weather Research and Forecasting (WRF) model by using detrending followed by the 1-D fast Fourier transform (FFT). Presented spectra from a high-resolution WRF simulation are characterised by mesoscale energy distribution similar to that derived from the aircraft measurements (Nastrom and Gage, 1985; Lindborg, 1999); the slope of the WRF spectrum is close to $-5/3$ in the free troposphere at scales smaller than 400 km and to $-3$ at larger scales.

Our discussion is focused on the application of the LAM ALADIN (Aire Limitée Adaptation dynamique Développement InterNational; Fischer et al., 2005) which is extensively used for the operational NWP in Europe and North Africa. In the case of ALADIN and closely related models AROME and HARMONIE, as well as the spectral HIRLAM model (Gustafsson and McDonald, 1996), both issues in the computation of energy spectra, the aperiodicity and the transform, are a priori handled because ALADIN is a spectral model which applies a bi-Fourier transform in the $x$ and $y$ directions of the grid-point value matrix, with a quasi-isotropic truncation in spectral space. The spectral dynamics is particularly suitable for the mesoscale data assimilation which applies vorticity and divergence variables instead of the velocity components (Berre, 2000; Gustafsson et al., 2001; Fischer et al., 2005). The biperiodicity is obtained by extending prognostic fields over an artificial narrow zone along the model eastern and northern boundaries which makes the fields periodic (Haugen and Machenhauer, 1993). The extension zone is considered a purely mathematical device with negligible impact on model equations and it is usually included in the kinetic energy spectra of dynamical fields and in the spectra of the forecast-error variances used in data assimilation. Such spectra are regularly used in studies of the model performance (e.g. Horvath et al., 2011) and for tuning of the model numerics (e.g. Váña et al., 2008) and physics (e.g. Bengtsson et al., 2012).

The main question we ask is about the contribution of divergent kinetic energy to the total kinetic energy in ALADIN as a function of the horizontal scale and altitude. While Koshyk et al. (1999) and Burgess et al. (2013) discussed this question for the upper troposphere and the stratosphere in the global models of lower resolution, we focus on the middle and the lower troposphere around 100 km and smaller. The main result is the ratio between divergent kinetic energy and the total kinetic energy in a typical mid-latitude mesoscale model of resolution around 4 km. We compare the energy partitioning obtained following the standard ALADIN biperiodisation procedure and the detrending method outlined in Errico (1985) and we show that the same result concerning the percentage of divergent energy in mesoscale motions in ALADIN is obtained for the two biperiodisation methods.

The reminder of the paper is organised as follows. Section 2 describes the applied model, the dataset and the computation of spectra. Section 3 presents the results along with a comparison of two biperiodisation techniques. The summary and the conclusions are provided in section 4.

## 2. Model and data analysis

### 2.1. The ALADIN model configuration

The analysis of spectra is performed using the 6-hour ALADIN forecasts, obtained from the operational version of ALADIN model in Slovenia (ALADIN/SI). The investigation period is July 2007 and two runs per day are used. The model domain (Fig. 1) is centred over Slovenia and covers most of continental Europe and the central part of the Mediterranean. The domain dimensions are $L_x = 1930$ km and $L_y = 1850$ km in the zonal and meridional directions, respectively. The number of model grid points is 439 in the $x$ direction and 421 in the $y$ direction. The black line in Fig. 1 denotes the edge of the physically relevant domain. The total model domain extends in each direction for additional 11 points which define the extension zone, so-called E-zone (Haugen and Machenhauer, 1993). Thus the computational model domain consists of $N_x = 450$ points along the $x$ and $N_y = 432$ points along the $y$ direction with values of $N_x$ and $N_y$ tuned for the application of FFT. The horizontal grid spacing is $\Delta x = \Delta y = 4.4$ km. The model version is CY35T1 that includes the most recent ALARO physics package (Gerard et al., 2009). The ALADIN vertical coordinate is the terrain-following hydrostatic pressure coordinate with 43 levels up to 5 hPa. The top boundary condition is determined by setting the vertical velocity to zero ($\omega = 0$). The model uses the elliptic truncation of the bi-Fourier series to provide a uniform resolution in the $x$ and $y$ directions which means that only the wavenumbers $k$ and $l$ that satisfy the equation $(k/N_k)^2 + (l/N_l)^2 \leq 1$ are considered. Here, $N_k$ and $N_l$ are the maximal wavenumbers in the zonal and meridional directions, respectively, which are in our case $N_k = 225$ and $N_l = 216$. Opposite to the linear grid used for dynamical fields ($N_k = N_x/2$), the model orography is truncated at $3\Delta x$ in order to prevent aliasing related to the computation of the pressure gradient force in orographic regions. The extension of prognostic fields over the E-zone is performed by using a spline function as described in the Appendix. Further details about the ALADIN model are available at http://www.cnrm.meteo.fr/aladin and numerous references therein.

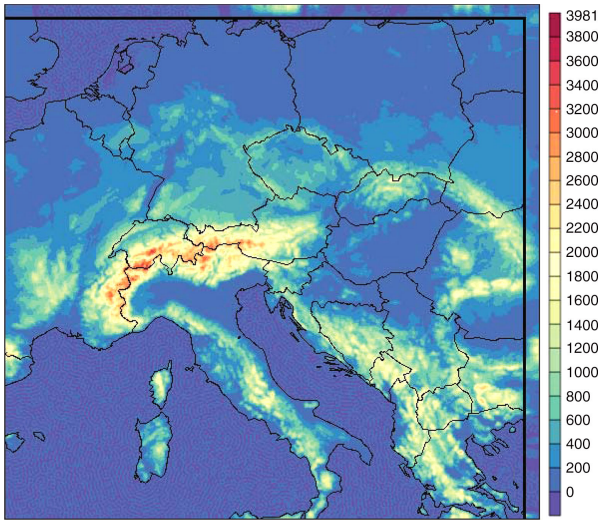


*Fig. 1.* The model domain and orography. The border of the extension zone is denoted with the black line.

Like in all NWP models, the results at small scales are influenced by the applied horizontal diffusion. For example, Skamarock (2004) illustrated a strong impact of the numerical dissipation applied in the WRF model on the shape of the spectra at small scales. Bengtsson et al. (2012) showed how the tuning of the horizontal diffusion in HARMONIE, which is a non-hydrostatic version of ALADIN at a higher resolution, greatly affects the simulated precipitation. The semi-Lagrangian horizontal diffusion applied in ALADIN is described in Vàña et al. (2008). We do not attempt to discuss the impact of the horizontal diffusion on our results; we make use of the model version used operationally which presumably applies the latest parameterisations and produces the best forecasts.

Integrations of 6-hour length are performed in the so-called downscaling or dynamical adaptation mode, which means that the initial conditions are supplied by ECMWF analyses. The lateral boundary conditions are applied with 3-hour frequency. The time step for the semi-Lagrangian integration is 180 seconds. Their horizontal and vertical interpolation to the ALADIN grid is followed by a digital filter initialisation (Lynch and Huang, 1992). The applied initial and boundary conditions are obtained from an ECMWF 4-D-Var ensemble that otherwise consists of 20 members and was prepared by using perturbed observations, sea-surface temperature and 2-m relative humidity (Isaksen et al., 2007; Zagar et al., 2013). The analyses are the results of a 12-hour 4-D-Var that applies one T95 inner loop minimisation (70 iterations) and a T255 outer loop. All 20 members are downscaled in the same way for the purpose of the background-error variance modelling. The results presented here are based on downscaling the first ensemble member; we checked that the spectra obtained by averaging all ensemble members do not differ from the spectra of an individual ensemble member.

### 2.2. Computation of the spectra

The Fourier transform pair for the zonal wind component ($u$) in ALADIN is defined as:

$$\hat{u}^z_{kl} = \frac{1}{N_x N_y} \sum_{i_x=1}^{N_x} \sum_{i_y=1}^{N_y} u(i_x, i_y, z) \exp(-2\pi i(\frac{k i_x}{N_x} + \frac{l i_y}{N_y})) \quad (1)$$

$$u(i_x, i_y, z) = \sum_{k=-N_k}^{N_k} \sum_{l=-N_l}^{N_l} \hat{u}^z_{kl} \exp(2\pi i(\frac{k i_x}{N_x} + \frac{l i_y}{N_y})), \quad (2)$$

where $x$, $y$ and $z$ define the zonal, meridional and vertical indices in physical space, $k$ and $l$ are zonal and meridional wavenumbers and $\hat{u}^z_{kl}$ is a bi-Fourier spectral coefficient.

The dynamical fields in ALADIN are saved in terms of the spectral expansion coefficients $\hat{u}^z_{kl}$, $\hat{v}^z_{kl}$, making the computation of the kinetic energy ($E_K$) spectra straightforward. From the Parseval theorem

$$\frac{1}{L_x L_y} \int_{-L_x/2}^{L_x/2} \int_{-L_y/2}^{L_y/2} [u(x,y)^2 + v(x,y)^2] dx dy = \sum_{k=-\infty}^{\infty} \sum_{l=-\infty}^{\infty} (\hat{u}_{kl} \hat{u}_{kl}^* + \hat{v}_{kl} \hat{v}_{kl}^*), \quad (3)$$

the kinetic energy in the wave component ($k$,$l$) at level $z$ is obtained as

$$E^z_{kl} = \frac{1}{2} (\hat{u}^z_{kl} \hat{u}^{z\,*}_{kl} + \hat{v}^z_{kl} \hat{v}^{z\,*}_{kl}). \quad (4)$$

The total kinetic energy for the total horizontal wavenumber $K$ ($K^2 = l^2 + k^2$) is obtained by the summation of $E_{kl}$ over wavenumber bands $K - \Delta K/2 K \le K + \Delta K/2$, where $K = 2\pi n / L_x$ with $n = 1,2,3, \ldots$ and $\Delta K$ is the difference between two successive wavenumbers.

To obtain the rotational and divergent kinetic energy spectra, the following steps are made: first, the spectral coefficients of the vorticity and divergence fields are computed at each model level as derivatives of the velocity components:

$$\widehat{\delta}^z_{kl} = ik\hat{u}^z_{kl} + il\hat{v}^z_{kl} \quad (5)$$

$$\widehat{\zeta}^z_{kl} = ik\hat{v}^z_{kl} - il\hat{u}^z_{kl}. \quad (6)$$

Here, $\widehat{\zeta}^z_{kl}$ and $\widehat{\delta}^z_{kl}$ represent the spectral coefficients of vorticity and divergence, respectively, * stands for the complex conjugate operator and $i$ denotes the imaginary unit. By summing up eq. (5) multiplied by $\widehat{\delta}^{z\,*}_{kl}$ and eq. (6) multiplied by $\widehat{\zeta}^{z\,*}_{kl}$, we obtain

$$\widehat{\zeta}^z_{kl} \widehat{\zeta}^{z\,*}_{kl} + \widehat{\delta}^z_{kl} \widehat{\delta}^{z\,*}_{kl} = (k^2 + l^2)(\hat{u}^z_{kl} \hat{u}^{z\,*}_{kl} + \hat{v}^z_{kl} \hat{v}^{z\,*}_{kl}). \quad (7)$$

Thus the kinetic energy in the wave component ($k$, $l$) can be written as

$$E^z_{kl} = \frac{1}{2} \frac{\widehat{\zeta}^z_{kl} \widehat{\zeta}^{z\,*}_{kl} + \widehat{\delta}^z_{kl} \widehat{\delta}^{z\,*}_{kl}}{k^2 + l^2}. \quad (8)$$

The divergent and the rotational parts of the kinetic energy are thus defined as follows:

$$E^z_{DIV,kl} = \frac{1}{2} \frac{\widehat{\delta}^z_{kl} \widehat{\delta}^{z\,*}_{kl}}{k^2 + l^2} \quad (9)$$

$$E^z_{VOR,kl} = \frac{1}{2} \frac{\widehat{\zeta}^z_{kl} \widehat{\zeta}^{z\,*}_{kl}}{k^2 + l^2}. \quad (10)$$

Equations (9) and (10) are equivalent to similar equations for the global spectral models (e.g. Koshyk and Hamilton, 2001). Energy is expressed in units $m^2 s^{-2}$ or $Jkg^{-1}$. In other words, our spectra for different layers are not mass weighted, which is not seen as a problem for a study focused on the divergent energy contribution to total kinetic energy. We shall refer to the results produced by following eqs. (5)–(10) as the ALADIN method. The derived spectra include a certain level of artificial energy added by the E-zone. As discussed earlier, the ALADIN dynamics and data assimilation systems have been successfully developed by using the E-zone and by applying eq. (4) for the computation of the kinetic energy spectra. The impact of the E-zone was addressed in the context of model performance and data assimilation in the HIRLAM model by Gustafsson and McDonald (1996) and Gustafsson et al. (2001), respectively.

For the application of the detrending procedure, vorticity and divergence fields obtained by eqs. (5) and (6) are transformed to grid-point space by the inverse FFT. In this step the E-zone is included as otherwise the stored spectral fields and eqs. (5) and (6) could not be applied. Once vorticity and divergence are obtained in grid-point space, the E-zone is removed from consideration. Biperiodicity is achieved following Errico (1985) which includes the computation of the linear trend from the end points along each row and column of data followed by the removal of the trend. The procedure leaves zeroes at the boundaries of the 2-D fields. These fields are then transformed back to spectral space by FFT and the rotational and divergent $E_K$ spectra are computed by eqs. (9) and (10). The results obtained in this way are referred to as the detrending method.

Note also that the same dimensionless $K$ applies to somewhat different scales in the two methods as the domain in the case of the ALADIN method is about 48 km wider in each horizontal direction. This, and an easier discussion are reasons that $E_K$ is shown as a function of the horizontal wavelength $\lambda$ ($\lambda = 2\pi/K$), rather than usually used wavenumber. The parameter $\lambda$ will be referred to as scale. We assume that the choice of the appropriate method

for the computation of the trend and aliasing of larger scales onto small scales on average equally effect vorticity and divergence so that their ratio is not significantly affected by these problems. Similarly, we can assume that the potential impact of the E-zone on the rotational and divergent $E_K$ spectra is about equally large.

The ALADIN method presents obvious advantages for the computation of the spectra in the NWP framework and for the model development. At the same time, there is a possibility of the impact of artificial energy on the shape of the spectra, especially for scales of our interest around 100 km. On the other hand, Errico (1987) and Van Tuyl and Errico (1989) discussed shortcomings of the detrending approach. Whereas their discussion was of a more qualitative type, Frehlich and Sharman (2008) provided a more fundamental discussion of the detrimental impacts of detrending and spectral decomposition on the energy spectra for small scales. These authors evaluated the spectra for levels between 9 km and 11 km for several NWP models and compared them with theoretically calculated spectra for various averaging lengths. The comparison of NWP models with the spectral model of Lindborg (1999) and theoretically calculated spectra showed that in the applied models with the horizontal resolution about 10 km, spectra already started to deviate from the Lindborg model at several hundred km. In addition, the spectra derived by using the linear detrending and the spectral decomposition are shown to be more sensitive to the small-scale statistics and likely to contain enhanced energy at the smallest scales in comparison to their theoretical equivalents. The negative impact of detrending has previously been discussed also by Denis et al. (2002) who proposed the discrete cosine transform as an alternative way for achieving biperiodisation.

The spectra of kinetic energy obtained by the two biperiodisation methods are not quantitatively comparable. The ALADIN method provides the total kinetic energy in wave motions in the model domain while the spectra resulting from the detrending approach describes the spectral distribution of flow variance. Furthermore, spectra obtained from eq. (8) are not the same as those obtained from eq. (4) as by applying eqs. (5) and (6) we have lost the energy contribution from the domain-average wind ($k = l = 0$ contribution). This affects also the spectra computed by the detrending approach. An example of the spectra obtained from eq. (4) and eq. (8) is compared in Fig. 2(a) for a randomly chosen date and level in the free troposphere. A difference between kinetic energy computed by eq. (8) and by eq. (4) is clearly seen at the largest resolved scales. The difference reduces as the scale decreases and below 100 km the difference steadily decreases from about 10% towards zero. It can also be seen in Fig. 2(a) that a randomly chosen level and date produces a smooth energy spectrum with a shape similar to the Lindborg model. The difference between the spectra computed from the velocity components and from vorticity and divergence, averaged across all levels and over the study period is presented in Fig. 2(b) for both the ALADIN and the detrending method. The results for the two methods are quite similar and similar to the above described random case. We focus our study on the scales smaller than 300 km for which the difference is below 20%.

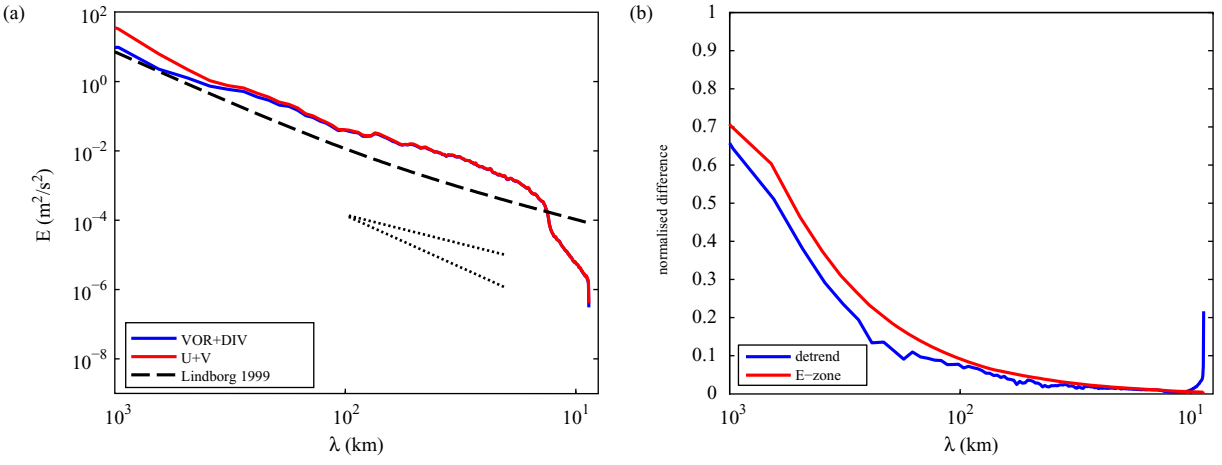


*Fig. 2.* (a) A kinetic energy spectrum, obtained as a sum of rotational and divergent energy and a spectrum obtained from $u$ and $v$ wind components at a model level close to 530 hPa. A randomly selected date is 20 July, 18 UTC run, 6-hour forecast and the spectra are produced by the detrending procedure. Short dotted lines have slopes $K^{-3}$ and $K^{-5/3}$. The dashed line is Lindborg (1999) functional fit [eq. (71)] to aircraft observations. (b) The difference between kinetic energy computed from the wind components and from rotational and divergent energy using the two biperiodisation techniques normalised by the kinetic energy computed from the wind components. The result is averaged over all model levels and over one-month period.

Forecasts are generated for each day of the one-month period at 6 and 18 UTC. An inspection of the time evolution of the spectra at the smallest resolvable scales shows that the initial energy growth, referred to as spin-up, is largest during the first three hours of forecasts initialised after applying the digital filtering. During 3-hour to 6-hour forecasts changes of the spectra are minor and thus we use 6-hour forecasts. No significant difference between the runs started at 06 and at 18 UTC was observed; therefore averaging over both runs was applied, as well as a monthly average.

## 3. Distribution of rotational and divergent energy in ALADIN

We begin the discussion by presenting the rotational and divergent energy spectra, obtained from the detrending method. These spectra can be compared with other available mesoscale model spectra (e.g. Skamarock, 2004; Skamarock and Klemp, 2008). Results are averaged for three layers defined as the 'stratosphere' (11 model levels between 5 and 250 hPa), the 'free troposphere' (21 model levels between 250 and 850 hPa) and the 'planetary boundary layer' or 'PBL' (11 model levels below 850 hPa). The average top altitudes of these layers are 36 km, 10 km and 1300 m for the stratosphere, the free troposphere and the PBL, respectively. All computations are performed on model levels to avoid any interpolation. In figures, the hydrostatic height pressure is used on the ordinate axis to make discussion easier. The spectra of total $E_K$ reveal properties found in earlier studies. However, our discussion is focused on differences between the divergent and rotational $E_K$ spectra at scales which have not been studied earlier. After presenting average properties of the $E_K$ spectra we continue with a more detailed presentation of the vertical and horizontal distribution of divergent energy with respect to total kinetic energy based on the two biperiodisation methods.

### 3.1. Horizontal spectra

We start by showing spectra averaged over four model levels between 9 and 11 km where most of the aircraft data used in Lindborg (1999) and Nastrom and Gage (1985) were collected. It can be seen in Fig. 3 that in the mesoscale region of our interest, the total $E_K$ spectrum is very well described by the analytical fit to the data derived by Lindborg (1999). The departure from the Lindborg model occurs between 30 and 20 km scale. Following Skamarock (2004) and Frehlich and Sharman (2008), we conclude that the effective resolution of the applied ALADIN/SI model is about 6–7$\Delta x$. For this reason, we shall be computing the

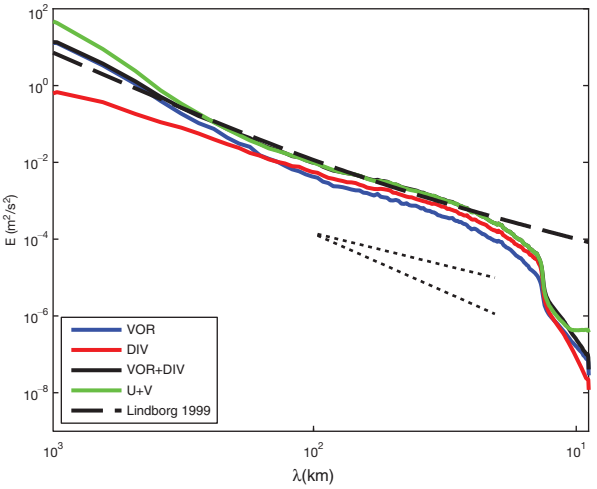


*Fig. 3.* Energy spectra averaged over model levels between 9 and 11 km. VOR denotes rotational kinetic energy (blue line), DIV divergent kinetic energy (red line), VOR + DIV denotes total kinetic energy as a sum of the rotational and divergent components (black line) whereas U + V stands for the total kinetic energy computed from the velocity components (green line).

linear fit of mesoscale spectra for scales greater than 30 km. At the scale corresponding to 3$\Delta x$, the cut-off scale for the model orography, a sharp energy fall-off takes place. We can also notice that the kinetic energy spectrum, obtained as a sum of rotational and divergent components is below 200 km nearly the same as the spectrum calculated from the velocity components.

If we focus on the spectra of rotational and divergent kinetic energy, we first observe a shallower slope of the divergent energy over all scales. A distinct feature in Fig. 3 is the crossing point of $E_{DIV}$ and $E_{VOR}$ located at about 150 km scale. At scales smaller than 150 km divergent energy dominates over rotational energy and their relative difference appears rather steady over scales smaller than 100 km. The location of the crossing point approximately matches the location where the $E_K$ spectrum changes the slope; the linear fit of $E_K$ for scales between 150 and 30 km gives a slope $-1.9$ which is somewhat steeper than the observed slope $-1.7$ (i.e. $-5/3$; Nastrom and Gage, 1985). Below 150 km, the slope of $E_{DIV}$ spectrum is close to $-1.8$ while the $E_{VOR}$ spectrum has a slope about $-2$. For larger scales, the difference between the slopes of divergent and rotational spectra is clearly increasing as the horizontal scale becomes larger as found in the global model data studied by Burgess et al. (2013) and in the analysis of global rotational and inertio-gravity energy by Zagar et al. (2009, 2010).

In Fig. 4 we take a closer look at the three atmospheric layers. On average, the spectra are shallowing towards the surface. The slopes of the total $E_K$ spectra, fitted between 150 and 30 km, are $-1.5$, $-1.8$ and $-1.9$ for the

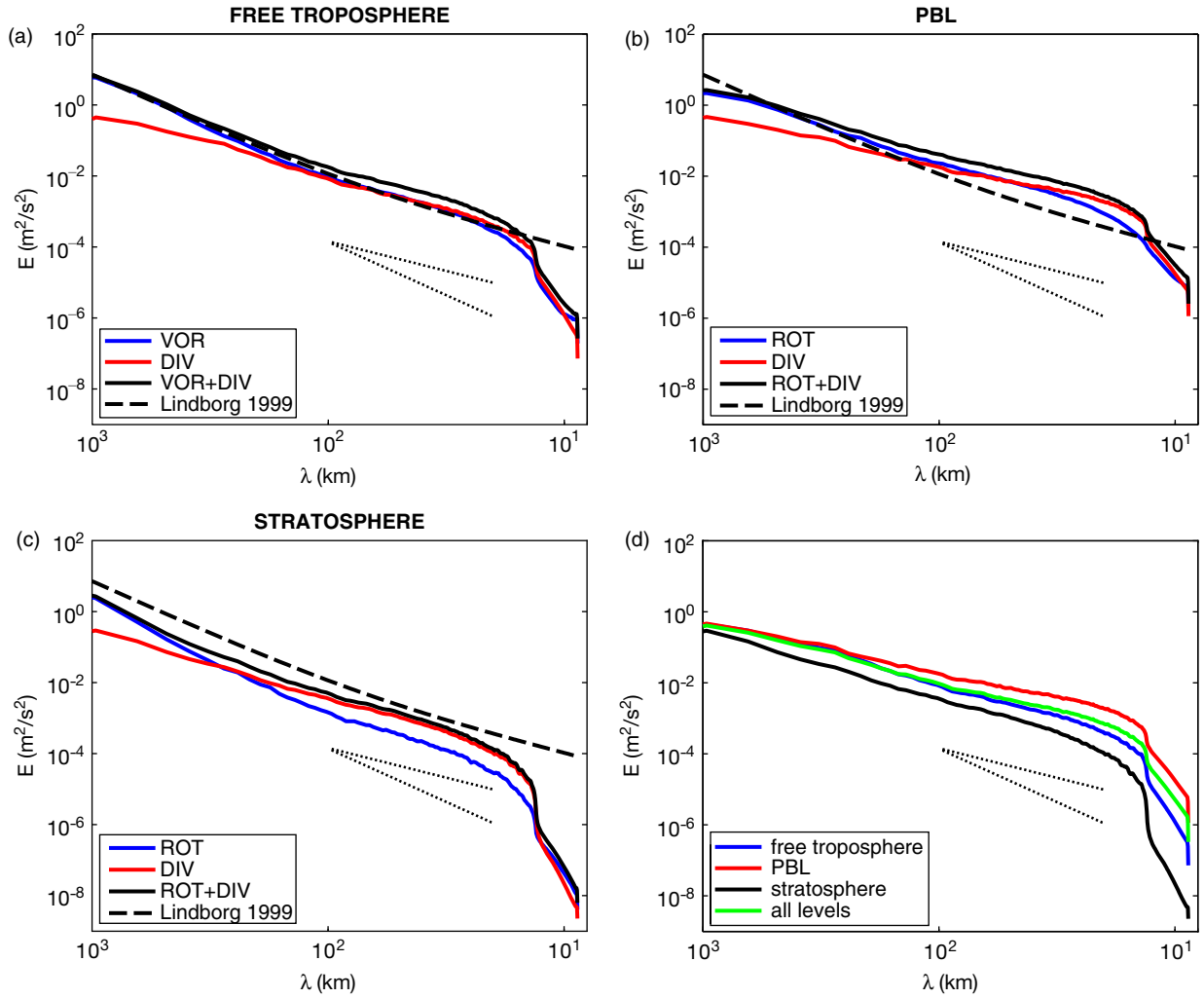


*Fig. 4.* Monthly and vertically averaged spectra of rotational (blue), divergent (red) and total kinetic energy (black) in (a) the free troposphere, (b) the planetary boundary layer (PBL) and (c) the stratosphere. (d) Divergent kinetic energy in various layers.

PBL, the free troposphere and the stratosphere, respectively. The PBL spectrum is shallower than the orography spectrum which in ALADIN has slope of $-1.8$ (Fig. 5). This value is between the referent slope of $-1.7$ and the global orography spectrum $K^{-2}$ (e.g. Balmino, 1993). Different energy levels in PBL are associated with bottom boundary forcings and related physical processes. The slope of the energy spectrum in NWP models is always influenced by the applied horizontal diffusion (e.g. Skamarock, 2004; Vàña et al., 2008). Diagnosis of the exact impact of various physical and non-physical forcings on the slope of spectra in ALADIN is, however, outside the scope of the present study. Another evidence of orography forcing in all layers is the energy fall-off at $3\Delta x$ rather than at $2\Delta x$ cut-off applied for model numerics.

In Fig. 6 it is noticeable that the variance associated with the computed spectra is significant. The magnitude of the standard deviation is similar to the energy levels. This applies to all scales although the variance somewhat increases as the scales get larger. This result is consistent with the variance level found in the WRF model (Skamarock, 2004) and in the GASP observations in Nastrom and Gage (1985). Fig. 6 also shows that variance is nearly the same for the rotational and divergent kinetic energy in the free troposphere. In the stratosphere the difference between divergent and rotational energy variance at large scales is greater than in the free troposphere and in the PBL (not shown), suggesting that a larger input data sample might reduce variance.

A common feature of the spectra in all layers is the dominance of divergent energy over rotational energy on scales below 100 km. As a result, slopes of the spectra for divergent energy are everywhere shallower than the slopes for the rotational energy spectra (Fig. 7). There is a general although slight increase of the slope with height in both divergent and rotational spectra. For divergent energy, the

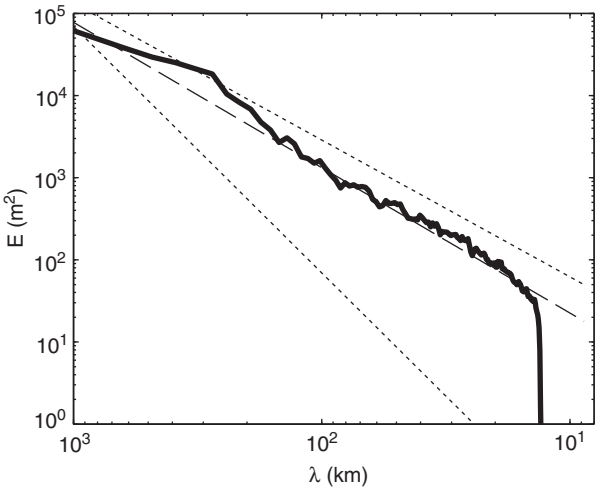


*Fig. 5.* Spectrum of the model surface geopotential height. The dotted lines are $K^{-3}$and $K^{-5/3}$, the dashed line is the best linear fit ($K^{-1.8}$).

increase of the slope is largest below 800 hPa, likely related to the surface forcings. Rotational energy has a more gradual increase in the PBL and a larger change between 500 and 300 hPa. Above 100 hPa, the slope of the spectra for both $E_{DIV}$ and $E_{VOR}$ variables increases steeply towards the model top. The transition from the vorticity-dominant to the divergence-dominant flow occurs at different scales in various layers (Fig. 4). In the boundary layer, the crossing scale at which divergent energy becomes greater than the rotational energy is found at about 50 km. A somewhat larger crossing scale is found in the free troposphere. On the contrary, the intersection point of the two spectra in the stratosphere is at nearly 300 km.

A more detailed vertical dependence of the crossing scale for the divergence dominance is provided in Fig. 8. Within the troposphere, there are two layers in which rotational energy is dominant all the way up to about 30 km scale. The first is at 450 hPa while the second altitude where vorticity-related flow dominates all the way up to 30 km scale is at about 900 hPa. In between these two points, in 600–700 hPa layer, divergent energy becomes prevalent at about 60 km. The vertical energy distribution is further discussed in the following section.

The upper part of Fig. 8 can be discussed in comparison with Burgess et al. (2013), who presented such analysis for the ECMWF model above 300 hPa (their Fig. 5d). In their study, the crossing scale at 300 hPa is located at nearly 100 km. From 300 hPa upward the scale becomes larger so that at 100 hPa the divergence becomes dominant at approximately 800 km. In our case, the crossing scale grows larger from 400 hPa towards 200 hPa. Above it, the scale is nearly constant, just like in Burgess et al. (2013) above 100 hPa. However, it is difficult to quantitatively compare the two datasets in the upper troposphere and stratosphere which in our case corresponds to the mid-latitude summer atmosphere whereas Burgess et al. (2013) studied global analyses in a winter month. Divergent energy in global analyses is mainly in the tropics and a relative increase of divergent energy towards 100 hPa in the global dataset most likely is associated with dynamics around the tropical tropopause. A general shallowing of all spectra towards the surface and the tropopause is in agreement with the idealised study by Tulloch and Smith (2009) based on a quasi-geostrophic model which produced transition of the spectra from $-3$ slope to $-5/3$ slope near the model boundaries (the surface and the tropopause).

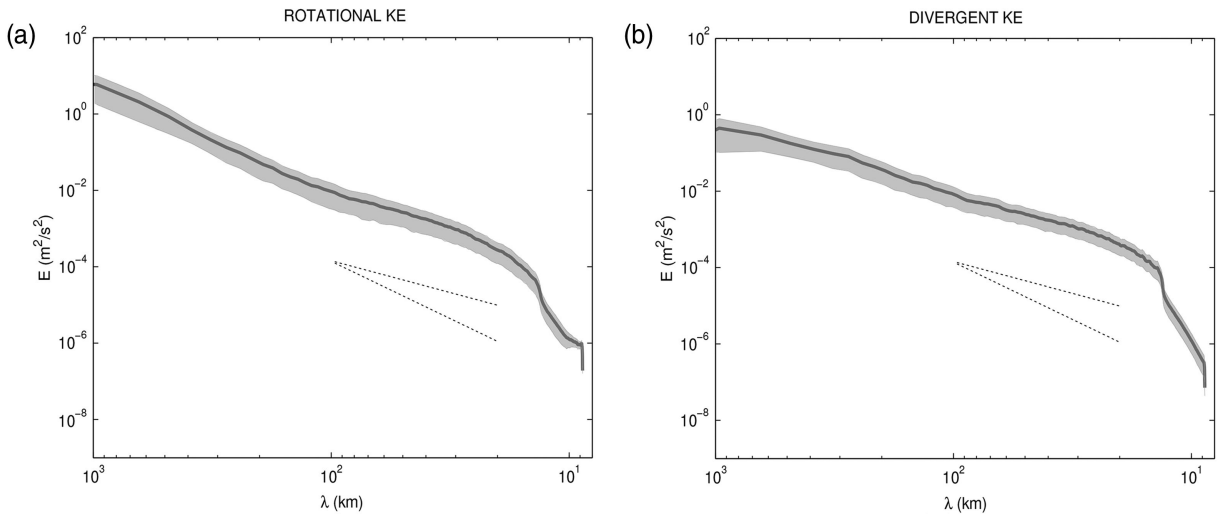


*Fig. 6.* Monthly and vertically averaged spectra of rotational (a) and divergent kinetic energy (b) in the free troposphere with the spread included. The shaded area encloses plus/minus one standard deviation.

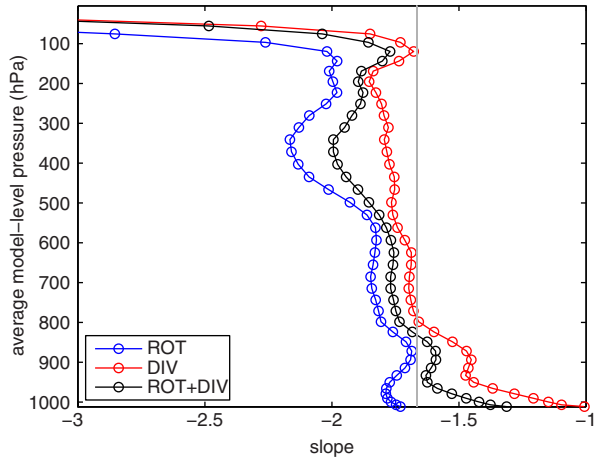


*Fig. 7.* The slope of the spectra of rotational (blue), divergent (red) and total kinetic energy (black) as a function of pressure. Spectra were fitted in the range between 150 and 30 km. The thin grey line represents $-5/3$.

If Fig. 8 is computed based on the standard ALADIN biperiodisation procedure, the shape of the curve remains the same until approximately 350 hPa. The slopes of divergent and rotational spectra in the upper troposphere and stratosphere proved difficult for the application of a linear fit because of the bump in the spectra at the scale corresponding to the width of the extension zone. This is the subject of ongoing investigation.

### *3.2. Quantification of the divergent kinetic energy contribution*

Now we quantify the contribution of divergent energy to the total kinetic energy as a function of altitude and horizontal scale. First, we discuss the distribution of divergent energy percentage based on the detrending method used to compute the spectra presented in the previous section and in other studies based on mesoscale NWP models. Then we compare the results with the ALADIN standard approach based on the E-zone.

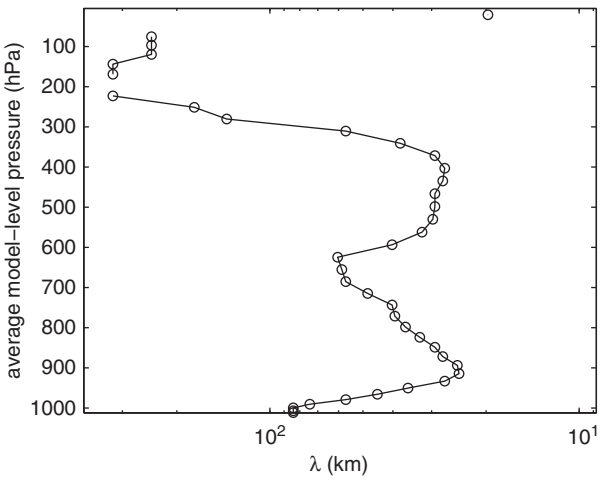


*Fig. 8.* The scale at which divergent kinetic energy exceeds rotational kinetic energy as a function of pressure.

The ratio between divergent and total kinetic energy in the three layers is presented in Fig. 9(a). There is a general increase of the divergent energy contribution as the scale becomes shorter in each of the three layers. For scales between 300 and 100 km, divergent energy represents 40–50% of the total energy in the free troposphere and PBL and 50–70% in the stratosphere. Below 100 km scale, the contribution of divergent energy in PBL continually increases as the scale becomes shorter until it reaches about 75% at the shortest resolved scale. An increase in the free troposphere is somewhat less steep. On the contrary, the divergent energy percentage in the stratosphere remains at about 75–80% level until the $3\Delta x$ scale where it sharply drops.

The result for the free troposphere can be compared with the results presented by Skamarock and Klemp (2008) for the $200 - 700$ hPa layer from the WRF model at nearly the same resolution. Skamarock and Klemp reported that the divergent energy component was two orders of magnitude smaller than the rotational component at largest scales represented by the model, was comparable to the rotational component at approximately 400 km scale and dominant below 30 km. In our study by using the ALADIN model, divergent energy in the free troposphere becomes dominant at 40 km scale and is comparable to rotational energy at all scales we consider for averaging ($\lambda < 300$ km). The results remain similar if we recompute the energy ratios for the 700–200 hPa layer used in Skamarock and Klemp (2008).

Even though divergent energy dominates over rotational energy in the stratosphere, it makes a rather small contribution to the total kinetic energy. This is presented in Fig. 9(b), which compares the relative role of divergent energy in various layers by showing the ratio between divergent energy in a selected layer and the total kinetic energy across all model levels. At scales larger than 100 km, the free troposphere contains the largest percentage of the divergent energy; an almost constant value of 20% of kinetic energy being divergent is present at all tropospheric scales between about 300 km and $3\Delta x$.

In the PBL the divergent energy contribution steadily increases as the scale becomes smaller and it reaches nearly 60% at the resolution limit. On the contrary, the stratospheric divergent energy contribution to the total atmospheric energy in ALADIN model is rather small – it presents less than 5% of the total energy. The curve representing the ratio between divergent energy across all levels and the total $E_K$ mimics the solution for the PBL;

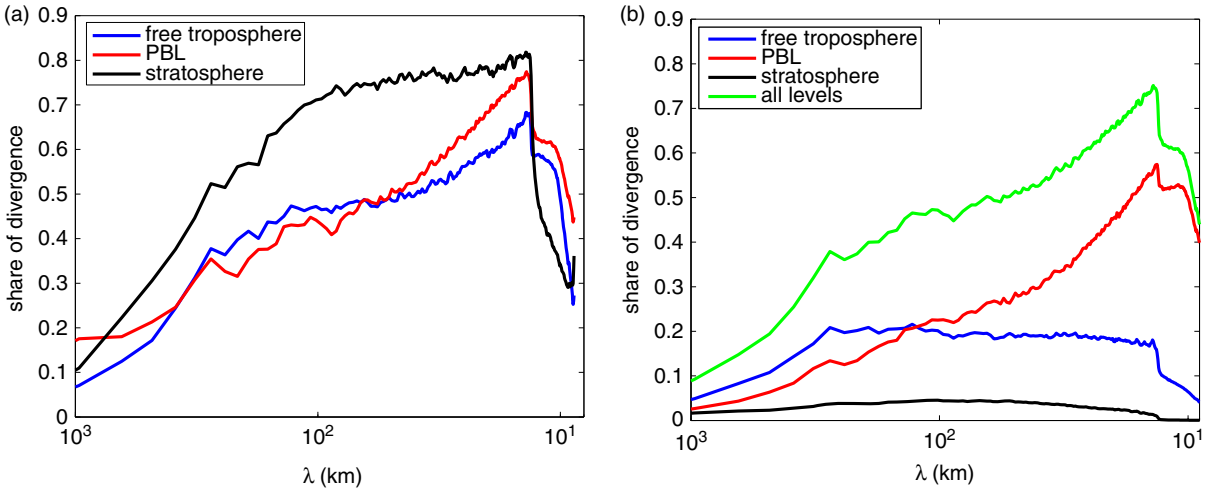


*Fig. 9.* (a) The fraction of divergent energy in the total kinetic energy in the same layer for stratosphere (black), free troposphere (blue) and PBL (red). (b) The fraction of divergent energy in the total kinetic energy across all model levels for stratosphere (black), free troposphere (blue), PBL (red) and all model levels (green).

it shows a nearly linear increase of the divergent energy contribution towards shorter scales. At the shortest resolvable scale in the ALADIN/SI model about three-quarters of the total kinetic energy is associated with divergent motions.

The sensitivity of the results with respect to the choice of levels included in different layers proves that the results shown in Fig. 9(b) are rather robust. Although the amount of divergence in the PBL varies with different numbers of layers included, the distribution of divergent energy percentages remains very similar to that shown in Fig. 9(b). For example, if we define the PBL as the levels below 950 hPa, the amount of divergence in the PBL represents less than 10% of energy at the large scales, but there is a rapid increase at scales below 100 km with a maximal value of nearly 50% at the smallest scales. In this case, divergence in the free troposphere represents a nearly constant contribution of about 25%. If the PBL is defined as levels below 700 hPa, the shape of the PBL divergence contribution remains similar but the percentage increases and it reaches up to 65% at the shortest scales. Divergent energy in the free troposphere in this case contributes about 10% of the total $E_K$.

Further insight into the vertical distribution of divergent energy as a function of scale is provided in Fig. 10, where the ratio between divergent energy and the total kinetic energy is presented as a function of horizontal scale and model level. This figure highlights details of several properties we have already mentioned. First of all, we notice a significant horizontal and vertical variability of the divergent energy percentage. The percentage of $E_{DIV}$ varies from 80% in the PBL below 20 km scale and in the stratosphere below 100 km to 10% and less above 500 km scales. The PBL maximum is due to the kinetic energy dissipation and therefore the largest values of divergent energy are found at levels close to the surface. There is a secondary maximum in the divergent energy percentage located at about 650 hPa. As seen earlier, the two fall-offs of energy occur at the orography cut-off scale $3\Delta x$ and at the cut-off scale for the numerics at $2\Delta x$. The $3\Delta x$ cut-off scale is particularly strongly seen in the stratosphere.

The most distinctive feature in Fig. 10 is the stratospheric maximum of divergent energy ratio. It is in agreement with other model-based studies pointing at the dominance of divergent energy in the stratosphere (e.g. Koshyk and Hamilton, 2001; Burgess et al., 2013) although they were using the lower resolution global data. The $E_K$ spectra based on observations in the stratosphere (Bacmeister et al., 1996) are characterised by a $-5/3$ slope in the range from 150 km to 600 km. The region of the strong vertical gradients in divergent energy present between 300 hPa and 100 hPa is most likely associated with the transition from troposphere to stratosphere. The dynamical mechanism responsible for the observed increase of $E_{DIV}$ should be vertically-propagating inertio-gravity waves. This was also the case for the baroclinic life-cycle simulation by Waite and Snyder (2009), who found that divergent kinetic energy dominates in the lower stratosphere.

If the divergent energy contribution to the total energy is averaged over all wavenumbers below 300 km scale, the profile of the mesoscale divergent energy fraction looks as presented in Fig. 11. It can be seen that below 900 hPa divergent energy on average represents more than 50% and its importance increases towards 70% at the surface. On average, about 50% of kinetic energy in the free troposphere is divergent. Above 400 hPa, the importance of

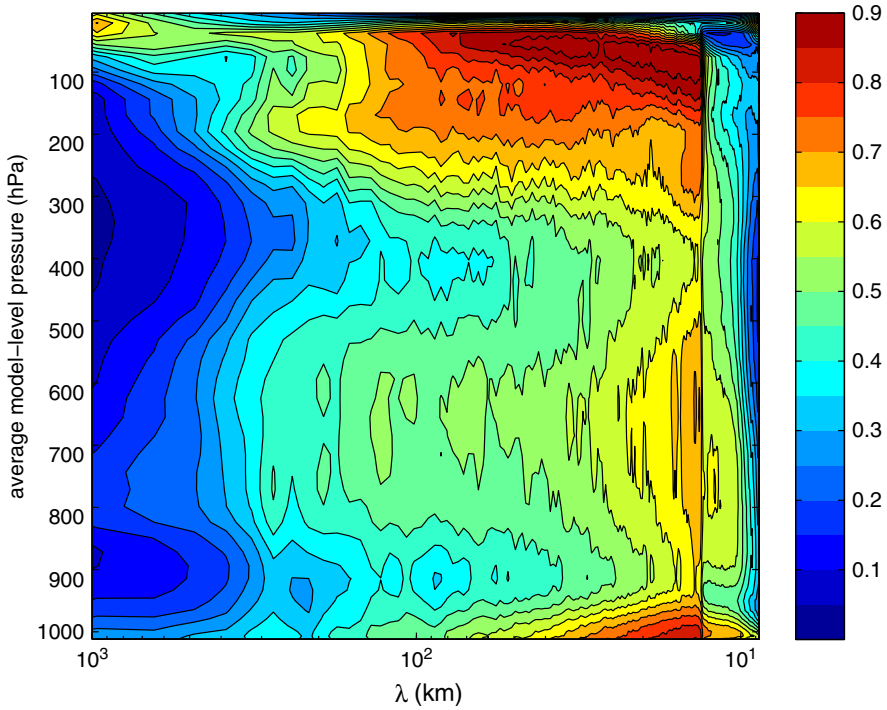


*Fig. 10.* Distribution of divergent energy contribution with respect to altitude and horizontal scale. Divergent energy is expressed as the fraction of the total kinetic energy at each model level. Contour interval is 0.05 (5%).

divergence increases towards 100 hPa level, where divergent energy makes again almost 70% of the total $E_K$. Above 50 hPa, the contribution of $E_{DIV}$ drops sharply towards zero at the model top.

The main properties of the results presented in Figs. 10 and 11 are robust to the applied method for the computation of divergent and rotational energies. This can be seen in Figs. 12 and 13 which are based on the ALADIN approach to the biperiodisation including the E-zone. First, Fig. 12 can be compared with Fig. 10. The difference produced by applying the two biperiodisation techniques is almost negligible in the PBL and small throughout the troposphere until about 400 hPa. In the upper troposphere and the stratosphere the relative percentage of the divergent energy on scales greater than 60 km is smaller in the ALADIN approach. This difference extends all the way to the larger scales. The reasons for difference are not completely clear and can be related to the properties of both methods, in particular the impact of the E-zone on scales greater than 50 km. Nevertheless, when the divergent energy contribution is averaged across scales smaller than 300 km, the vertical profile obtained from the ALADIN method is almost the same as the one obtained by applying the detrending method (Fig. 13). Therefore, using the extension zone for the biperiodisation does not influence our main conclusion concerning the divergent energy contribution to the total kinetic energy at mesoscale.

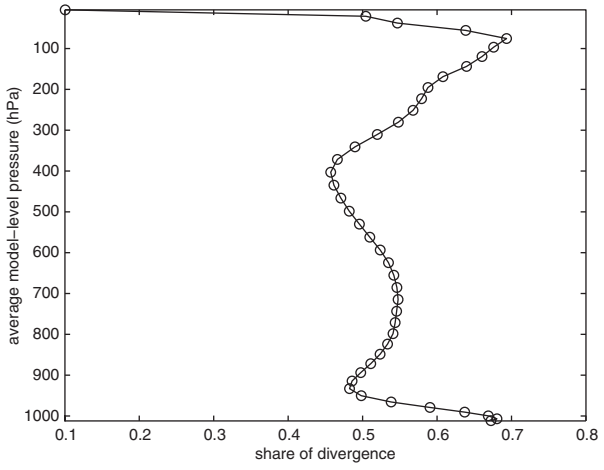


*Fig. 11.* Vertical distribution of the average fraction of divergent energy in the total kinetic energy. The averaging is done over the scales below 300 km.

## 4. Summary and conclusions

This study is motivated by a lack of understanding of the role of divergence in atmospheric energetics at scales around 100 km and smaller which are not resolved by the global NWP and climate models. Even though there is no exact equivalence between divergence and inertio-gravity

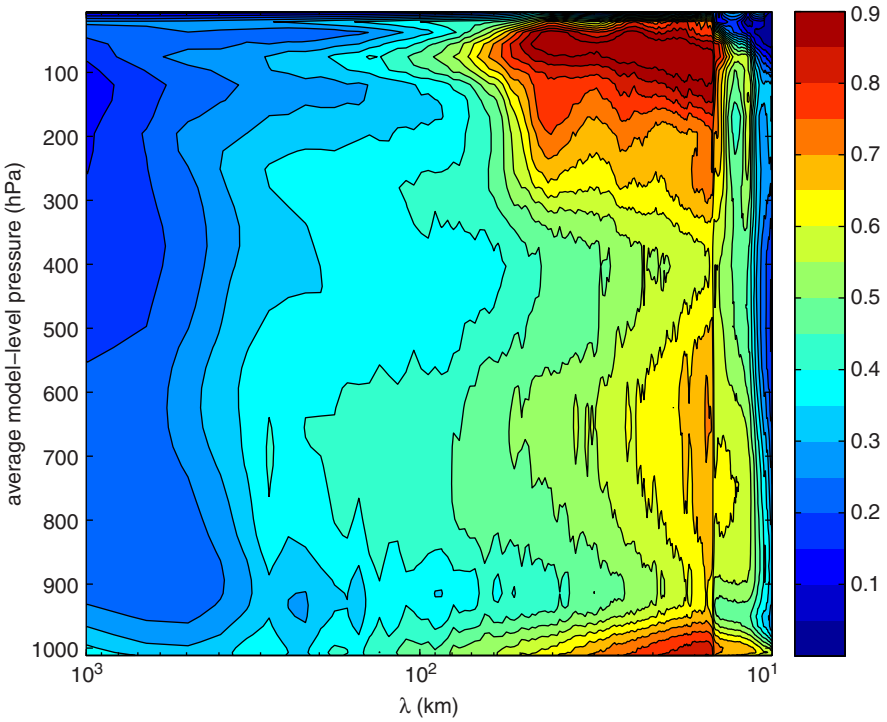


*Fig. 12.* Distribution of divergent energy contribution with respect to altitude and horizontal scale, based on the biperiodization using the extension zone.

flow on the one side and vorticity and quasi-geostrophic flow on the other, divergence can be considered as a good proxy for the inertio-gravity or unbalanced motions at subsynoptic scales in the mid-latitudes. The inertio-gravity part of the global kinetic energy has been estimated to about 10% of the total wave energy (Zagar et al., 2009, 2010). However, this applies to large scales where the inertio-gravity circulation is primarily due to the tropics and the largest orographical features of the planet. For the mid-latitude mesoscale case similar estimates of divergent energy and its temporal variability are not available. Furthermore, divergence is a control variable in data assimilation in mesoscale NWP models meaning that the energy spectra of analysis increments are greatly influenced by the imposed balance constraint in the background-error term for data assimilation. The behaviour of kinetic energy spectra due to assimilated mesoscale observations and dynamics of data assimilation in relation to the mesoscale model dynamics can be better understood if the kinetic energy spectra are split into divergent and rotational components. This provides a strong motivation for the computation of the rotational and divergent energy spectra in mesoscale NWP models.

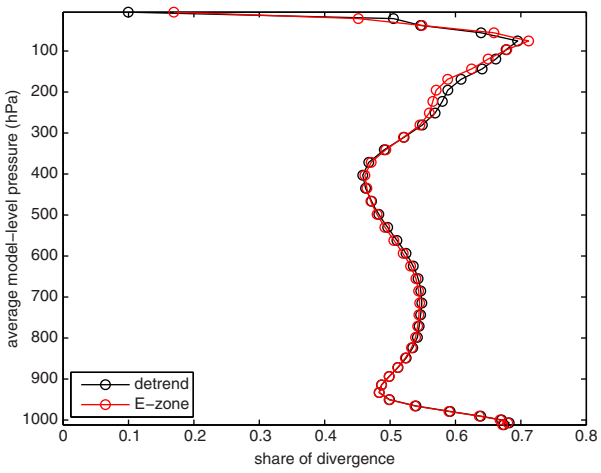


*Fig. 13.* Vertical distribution of the average fraction of divergent energy in the total kinetic energy for both biperiodization techniques.

The undertaken analysis of divergent and rotational kinetic energy spectra in the ALADIN/SI model is made complicated by two issues. First of all, the computation of the divergent and rotational kinetic energy spectra for a mesoscale model is a difficult problem. However, there is a natural way for doing this in the ALADIN model, which has biperiodic dynamical fields stored as complex coefficients of the 2-D Fourier decomposition. The second problem is that we are interested in motion scales and levels for which there are few observations present and which are known to be significantly influenced by the

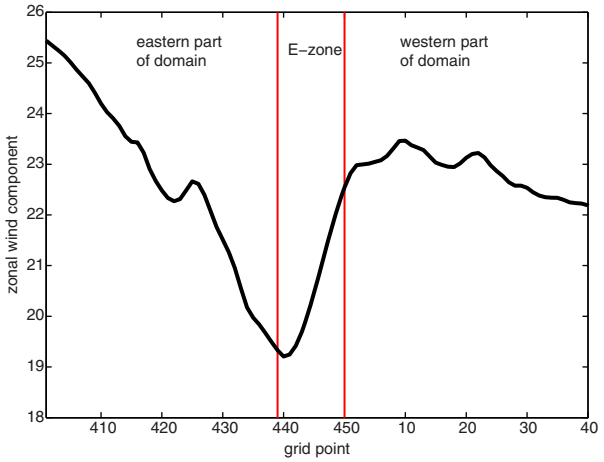


*Fig. A1.* Extension of the zonal wind component at model level close to 500 hPa for a random date and a random model-grid row.

applied horizontal diffusion (e.g. Skamarock, 2004; Bengtsson et al., 2012). Similar to studies based on global models, we apply the operational model results which represent the best dataset the model is capable to produce in its NWP application. We compare the results produced by the standard ALADIN approach for the spectra computation with that commonly used in mesoscale models based on detrending the velocity components data.

Within these limits, the following results are obtained. At scales below 300 km, about 50% of kinetic energy in the free troposphere is divergent energy. The percentage increases towards 70% at the surface and in the upper troposphere towards 100 hPa. This result is independent of the method applied for the biperiodisation of the velocity components in the limited area. The maximal percentage of divergent energy in the total kinetic energy at the same level is found at stratospheric levels around 100 hPa and at scales below 100 km, which are not represented by the global models analysed so far. This result calls for further studies with high-resolution models and comparisons with observations.

A detailed analysis of the vertical distribution of divergent energy revealed the scales at which divergent energy becomes greater than rotational energy. In two layers, at approximately 900 hPa and between 500 hPa and 400 hPa, rotational energy dominates on all scales larger than the model effective resolution found to be at about $6\Delta x$. At all levels, the divergent energy spectra are characterised by shallower slopes than the rotational energy spectra. Through most of the troposphere, the kinetic energy spectrum at scales around 100 km and smaller is reasonably well characterised by the $K^{-5/3}$ power-law while in the boundary layer, the spectrum becomes more shallow.

## 5. Acknowledgements

We would like to thank our ALADIN and HIRLAM colleagues Lisa Bengtsson-Sedlar, Magnus Lindskog, Nils Gustafsson, Neva Pristov and Filip Vàña, as well as Ted Shepherd for discussions of the spectra and models. We appreciate comments from three anonymous reviewers which helped to improve the paper. VB gratefully acknowledges the support of the Slovenian Research Agency through PhD funding. The Centre of Excellence for Space Sciences and Technologies SPACE-SI is an operation part financed by the European Union, European Regional Development Fund and Republic of Slovenia, Ministry of Higher Education, Science, Sport, and Culture.

## 6. Appendix

### *A.1. Biperiodisation in ALADIN*

The extension zone (E-zone, Fig. 1) is essential in making the limited area model ALADIN a spectral model. The biperiodic prognostic fields allow the application of FFT in the $x$ and $y$ directions. The extension is performed by using a spline function which takes into account values of the first two and the last two points in each row and column. The spline operator is applied first row by row and second column by column. The formulas for the row by row part are:

$$\begin{aligned} W_{i,j} = {} & W_{N_{xi},j} \\ & + N_i\left(\frac{W_{1,j} - W_{N_{xi},j}}{N} - \frac{N(2M_1 + M_2)}{6}\right. \\ & \left. + N_i\left(\frac{M_1}{2} + N_i\frac{M_2 - M_1}{6N}\right)\right) \end{aligned} \tag{11}$$

with

$$M_1 = \frac{2Z_1 - \frac{N}{N+1}Z_2}{4 - \left(\frac{N}{N+1}\right)^2}, \tag{12}$$

$$M_2 = \frac{2Z_2 - \frac{N}{N+1}Z_1}{4 - \left(\frac{N}{N+1}\right)^2}, \tag{13}$$

and

$$Z_1 = \left(\frac{W_{1,j} - W_{N_{xi},j}}{N} - W_{N_{xi},j} + W_{N_{xi}-1,j}\right)\frac{6}{N+1}, \tag{14}$$

$$Z_2 = \left(W_{1+1,j} - W_{1,j} - \frac{W_{1,j} - W_{N_{xi},j}}{N}\right)\frac{6}{N+1}. \tag{15}$$

Here, $W$ is a prognostic variable, $N_{xi}$ is the number of grid points in the $x$ direction without the extension zone, $N$ is the width of the extension zone ($N{=}N_x - N_{xi}{+}1$) and $N_i$ is the index of the current point within the extension zone.

An example of extension along $x$ axis is shown in Fig. A1 for the zonal wind at 500 hPa for a random case. It shows a

smooth transition of the wind velocity across the extension area. To ensure this smooth transition, the number of points in the extension zone must not be too small and at the same time, the number must be smaller than the number of degrees of freedom defined by the elliptic truncation in order to avoid Gibbs waves in the E-zone (Dragulanescu, 1995). In practice, the shape of the extension curves varies from a nearly flat towards a single wave. Following the biperiodisation, solutions over the extension zone are additionally smoothed by a 9-point weighted average for each point in the E-zone.

## References


Bacmeister, J. T., Eckermann, S. D., Newman, P. A., Lait, L., Chan, K. R. and co-authors. 1996. Stratospheric horizontal wavenumber spectra of winds, potential temperature, and atmospheric tracers observed by high-altitude aircraft. *J. Geophys. Res.* **101**(D5), 9441–9470.

Balmino, G. 1993. The spectra of the topography of the Earth, Venus and Mars. *Geophys. Res. Lett.* **20**, 1063–1066.

Barnes, S. L. 1986. On the accuracy of omega diagnostic computations. *Mon. Wea. Rev.* **114**, 1664–1680.

Bengtsson, L., Sander, T., Vàña, F. and Svensson, G. 2012. Impact of flow-dependent horizontal diffusion on resolved convection in AROME. *J. Appl. Meteor. Climatol.* **55**, 54–67.

Berre, L. 2000. Estimation of synoptic and mesoscale forecast error covariances in a limited-area model. *Mon. Wea. Rev.* **128**, 644–667.

Burgess, B. H., Erler, A. R. and Shepherd, T. G. 2013. The troposphere-to-stratosphere transition in kinetic energy spectra and nonlinear spectral fluxes as seen in ECMWF analyses. *J. Atmos. Sci.* **70**, 669–687.

Courtier, P., Andersson, E., Heckley, W., Pailleux, J., Vasiljevic, D. and co-authors. 1998. The ECMWF implementation of three dimensional variational assimilation (3D-Var). I: formulation. *Q. J. R. Meteor. Soc.* **124**, 1783–1807.

Denis, B., Côté, J. and Laprise, R. 2002. Spectral decomposition of two-dimensional atmospheric fields on limited-area domains using the discrete cosine transform (DCT). *Mon. Wea. Rev.* **130**, 1812–1829.

Dragulanescu, L. 1995. ARPEGE/ALADIN: double-periodization and coupling. *Aladin stay report (available in paper form from Meteo France)*.

Errico, R. M. 1985. Spectra computed from a limited area grid. *Mon. Wea. Rev.* **113**, 1554–1562.

Errico, R. M. 1987. A comparison between two limited-area spectral analysis schemes. *Mon. Wea. Rev.* **115**, 2856–2861.

Fischer, C., Montmerle, T., Berre, L., Auger, L. and Stefânescu, S. E. 2005. An overview of the variational assimilation in the ALADIN/France numerical weather-prediction system. *Q. J. R. Meteor. Soc.* **131**, 3477–3492.

Frehlich, R. and Sharman, R. 2008. The use of structure functions and spectra from numerical model output to determine effective model resolution. *Mon. Wea. Rev.* **136**, 1537–1553.

Gerard, L., Piriou, J.-M., Brožkova, R., Geleyn, J.-F. and Banciu, D. 2009. Cloud and precipitation parameterization in a meso-gamma scale operational weather prediction model. *Mon. Wea. Rev.* **137**, 3960–3977.

Gill, A. E. 1982. Atmosphere-Ocean Dynamics. Academic Press, International Geophysical Series, San Diego, **30**, 662 p.

Gustafsson, N., Berre, L., Hörnquist, S., Huang, X.-Y., Lindskog, M. and co-authors. 2001. Three-dimensional variational data assimilation for a limited area model. Part I: general formulation and the background error constraint. *Tellus A* **53**, 425–446.

Gustafsson, N. and McDonald, A. 1996. A Comparison of the HIRLAM gridpoint and spectral semi-lagrangian models. *Mon. Wea. Rev.* **124**, 2008–2022.

Haugen, J. E. and Machenhauer, B. 1993. A spectral limited-area model formulation with time-dependent boundary conditions applied to the shallow-water equations. *Mon. Wea. Rev.* **121**, 2618–2630.

Horvath, K., Bajić, A. and Ivatek-Šahdan, S. 2011. Dynamical downscaling of wind speed in complex terrain prone to bora-type flows. *J. Appl. Meteor. Climatol.* **50**, 1676–1691.

Isaksen, L., Fisher, M. and Berner, J. 2007. Use of analysis ensembles in estimating flow-dependent background error variance. *Proceedings of ECMWF Workshop on Flow-Dependent Aspects of Data Assimilation*. Reading, UK, 11–13 June, 2007, 65–86.

Keyser, D. A. and Johnson, D. R. 1984. Effects of diabatic heating on the ageostrophic circulation of an upper tropospheric jet streak. *Mon. Wea. Rev.* **112**, 1709–1724.

Koshyk, J. N., Boville, B. A., Hamilton, K., Manzini, E. and Shibata, K. 1999. Kinetic energy spectrum of horizontal motions in middle-atmosphere models. *J. Geophys. Res.* **104**, 27177–27190.

Koshyk, J. N. and Hamilton, K. 2001. The horizontal kinetic energy spectrum and spectral budget simulated by a high-resolution troposphere-stratosphere-mesosphere GCM. *J. Atmos. Sci.* **58**, 329–348.

Li, Z. J., Chao, Y. and McWilliams, J. C. 2006. Computation of the streamfunction and velocity potential for limited and irregular domains. *Mon. Wea. Rev.* **134**, 3384–3394.

Lindborg, E. 1999. Can the atmospheric kinetic energy spectrum be explained by two-dimensional turbulence? *J. Fluid Mech.* **388**, 259–288.

Lynch, P. 1988. Deducing the wind from vorticity and divergence. *Mon. Wea. Rev.* **116**, 86–93.

Lynch, P. 1989. Partitioning the wind in a limited domain. *Mon. Wea. Rev.* **117**, 1492–1500.

Lynch, P. and Huang, X.-Y. 1992. Initialization of the HIRLAM model using a digital filter. *Mon. Wea. Rev.* **124**, 1225–1242.

Nastrom, G. D. and Gage, K. S. 1985. A climatology of atmospheric wavenumber spectra of wind and temperature observed by commercial aircraft. *J. Atmos. Sci.* **42**, 950–960.

Parrish, D. F. and Derber, J. C. 1992. The national meteorological center's spectral statistical-interpolation analysis system. *Mon. Wea. Rev.* **120**, 1747–1763.

Skamarock, W. C. 2004. Evaluating mesoscale NWP models using kinetic energy spectra. *Mon. Wea. Rev.* **132**, 3019–3032.

Skamarock, W. C. and Klemp, J. B. 2008. A time-split nonhydrostatic atmospheric model for weather research and forecasting applications. *J. Comp. Phys.* **227**, 3465–3485.

Tulloch, R. and Smith, K.S. 2009. Quasigeostrophic turbulence with explicit surface dynamics: application to the atmospheric energy spectrum. *J. Atmos. Sci.* **66**, 450–467.

Van Tuyl, A. H. and Errico, R. M. 1989. Scale interaction and predictability in a mesoscale model. *Mon. Wea. Rev.* **117**, 495–517.

Vàña, F., Bènard, P., Geleyn, J-F., Simon, A. and Seity, Y. 2008. Semi-lagrangian advection scheme with controlled damping: an alternative to nonlinear horizontal diffusion in a numerical weather prediction model. *Q. J. R. Meteor. Soc.* **134**, 523–537.

Waite, M. L. and Snyder, C. 2009. The mesoscale kinetic energy spectrum of a baroclinic life cycle. *J. Atmos. Sci.* **66**, 883–901.

Žagar, N., Tan, D., Isaksen, L. and Tribbia, J. 2013. Balance properties of the short-range forecast errors in the ECMWF 4D-Var ensemble. *Q. J. R. Meteor. Soc.* **139**, in press.

Žagar, N., Tribbia, J., Anderson, J. L. and Raeder, K. 2009. Uncertainties of estimates of inertia-gravity energy in the atmosphere. Part I: intercomparison of four analysis systems. *Mon. Wea. Rev.* **137**, 3837–3857.

Žagar, N., Tribbia, J., Anderson, J. L. and Raeder, K. 2010. Corrigendum. *Mon. Wea. Rev.* **138**, 2476–2477.